

Femtosecond Electron Dynamics in Graphene Nanoribbons – A Nonequilibrium Green Functions Approach Within an Extended Hubbard Model

Jan-Philip Joost,* Niclas Schlünzen, and Michael Bonitz

A new approach to study the correlated femtosecond electron dynamics in finite graphene clusters, such as nanoribbons, is presented here. The systems are described by an extended Hubbard model that takes into account the overlap of adjacent orbitals and hopping between up to third-nearest neighbors. The model is solved by the nonequilibrium Green functions approach combined with different self-energy approximations, including the second-Born and GW self-energy, to take into account electronic correlations. The description allows us to predict the correlated nonequilibrium dynamics of excited graphene nanostructures of arbitrary geometry containing up to 100 carbon atoms for up to 25 fs.

1. Introduction

Since the first experimental discovery of its unique features in 2004^[1] the interest in graphene has grown rapidly. As the first truly two-dimensional material it exhibits a number of unique mechanical, optical, and electronic properties which make graphene a promising candidate for various technological applications of the future.^[2–6] However, as graphene is a semimetal, the absence of a band gap prevents the realization of next-generation graphene-based nanoelectronics.^[7] Therefore, large effort was put into creating semiconducting graphene materials that retain its remarkable transport properties. While some methods focus on substrate-induced^[8,9] or strain-induced^[10,11] band gaps, the most promising approach, at the moment, is obtaining a band gap through the effect of quantum confinement in finite graphene nanostructures^[12,13] such as graphene nanoribbons (GNRs). The electronic properties and especially the low energy spectrum of the π -electrons are strongly influenced by the edge structure of the nanoribbons. Depending on the shape of the edges one distinguishes between armchair graphene nanoribbons (AGNR) and zigzag graphene nanoribbons (ZGNR).

J.-P. Joost, N. Schlünzen, Prof. M. Bonitz
Institut für Theoretische Physik und Astrophysik
Christian-Albrechts-Universität zu Kiel
24098 Kiel, Germany
E-mail: joost@theo-physik.uni-kiel.de

 The ORCID identification number(s) for the author(s) of this article can be found under <https://doi.org/10.1002/pssb.201800498>.

DOI: 10.1002/pssb.201800498

A detailed understanding of these finite graphene nanostructures is of high importance for current research. Due to the recently developed new synthesis methods of graphene nanoribbons,^[14–18] the number of exciting experiments increased drastically over the last years.^[19–25] Therefore, an accurate theoretical description of these systems in nonequilibrium and particularly of their time-resolved spectral properties is needed. However, finite graphene nanostructures, especially in nonequilibrium, are extremely complex, inhomogeneous systems that put high requirements on any theory that attempts to describe them accurately. A proper

theory has to describe finite systems that are experimentally accessible. Such systems typically include up to 100 carbon atoms.^[17,26,27] Further, the approach has to take into account the finite overlap of the atomic orbitals and describe moderate electronic correlations. Additionally, the two-dimensional geometry of the graphene honeycomb lattice has to be modeled. Finally, the theory has to be able to describe the correlated nonequilibrium dynamics of the system for up to several femtoseconds within a reasonable amount of computational time. In conclusion, one has to find a model that allows for an accurate description of these systems while at the same time remains numerically manageable.

A method that fulfills all these requirements is the theory of real-time nonequilibrium Green functions (NEGF) due to Keldysh.^[28,29] It allows for a self-consistent dynamics of correlated electrons fully obeying conservation laws. The method contains a single input quantity – the self-energy Σ , see Section 3 – and would be exact if the exact $\Sigma = \Sigma[G]$ was used. But in practice, of course, approximations are used. Nevertheless, the accuracy of NEGF simulations has been carefully tested in recent years, for example, refs. [30,31], and – with the appropriate choice of the self-energy – allows for reliable and predictive simulations. At the same time, NEGF simulations are computationally demanding and the effort scales cubically with the basis dimension. A link between accuracy and low numerical effort is provided by using Hubbard-type lattice models, for example, ref. [32], and we will, therefore, follow this strategy in the present paper as well. At the same time we will improve the model compared to earlier simulations, by using an extended Hubbard model where the model parameters are provided by ab initio approaches as discussed in Section 2. Using this approach we obtain accurate ground-state results for graphene

nanoribbons including the band gap, the momentum dispersion and the spectral function. Further the first nonequilibrium results for the electron dynamics following a short laser pulse are presented and demonstrate the strength of the NEGF approach.

This paper is organized as follows. In Section 2, we introduce the extended Hubbard model and formulate a systematic many-body description on the mean-field level. This is extended to correlation effects in Section 3 where the NEGF approach is introduced. Our numerical results are presented in Section 4 starting with ground-state properties and concluding with correlated electron dynamics in response to a short laser pulse. We conclude with an outlook in Section 5.

2. Extended Hubbard Model

The elementary constituent of graphene is carbon, the sixth element of the periodic table. As such, it contains six electrons that are in the configuration $1s^2 2s^2 2p^2$ if the carbon is in the ground state. That is, two electrons are close to the nucleus and occupy the innermost $1s$ -shell while the other four fill the outer shells of the $2s$ and $2p$ orbitals. However, in the presence of other carbon atoms one electron from the $2s$ orbital is excited to the $2p$ orbital and forms covalent σ -bonds between the atoms. The quantum-mechanical superposition of the remaining $2s$ electron with n of the $2p$ states is called sp^n hybridization.^[33]

The structure of graphene is obtained by the planar sp^2 hybridization. The three hybridized orbitals are oriented in a plane and have mutual angles of 120° . This lets the carbon atoms arrange in a hexagonal structure, the so-called honeycomb lattice. The remaining unhybridized $2p_z$ orbital is oriented perpendicular to the plane. Due to the non-negligible overlap between these orbitals of adjacent atoms, they form the so-called π -bonds.^[34] These half-filled bands are responsible for most of graphene's interesting electronic properties.

2.1. Tight-Binding Model

A commonly used model when describing graphene-based systems is the tight-binding approximation (TB) which is easy to solve due to its simplistic nature.^[35] In this model, the aforementioned $2p_z$ atomic orbitals are a common choice for the underlying basis set $|\tilde{i}\rangle$ which, in general, is non-orthogonal. The non-vanishing overlap of these single-particle orbitals is taken into account by the overlap matrix

$$\tilde{S}_{ij} = \langle \tilde{i} | \tilde{j} \rangle \quad (1)$$

where the special case of an orthonormal basis is equivalent to $\tilde{S}_{ij} = \delta_{ij}$.

In the TB approximation the graphene system is described by the single-particle Hamiltonian

$$\hat{H}^{\text{TB}} = \sum_{ijkl} \tilde{S}_{ik}^{-1} \tilde{h}_{kl}^{\text{TB}} \tilde{S}_{ij}^{-1} |\tilde{i}\rangle \langle \tilde{j}| \quad (2)$$

with the corresponding matrix elements $\tilde{h}_{kl}^{\text{TB}} = \langle \tilde{k} | \hat{H}^{\text{TB}} | \tilde{l} \rangle$ which in general include the kinetic part and the on-site potential as

well as any possible external single-particle excitations. The Hamiltonian \hat{H}^{TB} possesses a complete set of orthonormal eigenstates $|\Psi_n\rangle$, which are given by a linear combination of the atomic orbitals $|\tilde{i}\rangle$,

$$|\Psi_n\rangle = \sum_i \tilde{a}_i^n |\tilde{i}\rangle \quad (3)$$

These eigenstates and the corresponding eigenvalues E_n of the Hamiltonian are determined by the stationary Schrödinger equation

$$\hat{H}^{\text{TB}} |\Psi_n\rangle = E_n |\Psi_n\rangle \quad (4)$$

which can be transformed into a generalized eigenvalue problem by multiplying from the left with the bra vector $\langle \tilde{j} |$ resulting in

$$\sum_i \langle \tilde{j} | \hat{H}^{\text{TB}} | \tilde{i} \rangle \tilde{a}_i^n = \sum_i \langle \tilde{j} | \tilde{i} \rangle \tilde{a}_i^n E_n \quad (5)$$

This set of linear equations can be written in matrix form as

$$\tilde{\mathbf{H}}^{\text{TB}} \tilde{\mathbf{A}} = \tilde{\mathbf{S}} \tilde{\mathbf{A}} \mathbf{E} \quad (6)$$

where $\tilde{\mathbf{H}}^{\text{TB}}$, $\tilde{\mathbf{A}}$, and $\tilde{\mathbf{S}}$ contain the matrix elements $\tilde{h}_{ji}^{\text{TB}}$, \tilde{a}_i^n , and \tilde{S}_{ji} , respectively. \mathbf{E} is a diagonal matrix with the eigenvalues E_n .

To solve Equation (6) one can apply the symmetric Löwdin orthogonalization^[37] which leads to a standard eigenvalue problem

$$\mathbf{H}^{\text{TB}} \mathbf{A} = \mathbf{A} \mathbf{E} \quad (7)$$

that is defined in a new orthogonal basis $|i\rangle$ which are denoted without a tilde. Both basis sets are connected by the square root of the overlap matrix via

$$|i\rangle = \sum_k |\tilde{k}\rangle \tilde{S}_{ki}^{-\frac{1}{2}} \quad (8)$$

Further, the matrices containing the matrix elements of the Hamiltonian and the expansion coefficients of the eigenstates transform as

$$\mathbf{H}^{\text{TB}} = \tilde{\mathbf{S}}^{-\frac{1}{2}} \tilde{\mathbf{H}}^{\text{TB}} \tilde{\mathbf{S}}^{-\frac{1}{2}} \quad (9)$$

$$\mathbf{A} = \tilde{\mathbf{S}}^{\frac{1}{2}} \tilde{\mathbf{A}} \quad (10)$$

Thus, in the TB approximation the system is defined by the matrix elements of the single-particle Hamiltonian $\tilde{h}_{ij}^{\text{TB}}$ and the overlap matrix \tilde{S}_{ij} .

A common way to get a set of parameters that closely reproduce the electronic properties of graphene and graphene nanostructures is to fit the resulting TB band structure against ab initio results of DFT calculations.^[35,36,38] In practice, often only the orbital overlap of up to the third-nearest-neighbor atoms is considered which results in seven fitting parameters. An illustration of the three nearest neighbors of a single site in a

graphene lattice is depicted in **Figure 1**. The resulting matrix elements of the Hamiltonian are then given by

$$\tilde{h}_{ij}^{\text{TB}} = -J(\delta_{ij}\tilde{E}_{2p} + \tilde{t}_{ij}) \quad (11)$$

where J is the hopping amplitude which is used for normalization, \tilde{E}_{2p} is the $2p_z$ on-site energy of a carbon atom and \tilde{t}_{ij} are the hopping matrix elements defined as

$$\tilde{t}_{ij} = \begin{cases} \tilde{t}_1, & \text{if } (i,j) \text{ is 1 NN} \\ \tilde{t}_2, & \text{if } (i,j) \text{ is 2 NN} \\ \tilde{t}_3, & \text{if } (i,j) \text{ is 3 NN} \\ 0, & \text{else} \end{cases} \quad (12)$$

In a similar fashion, the elements of the overlap matrix are given by three parameters as

$$\tilde{S}_{ij} = \delta_{ij} + \begin{cases} \tilde{s}_1, & \text{if } (i,j) \text{ is 1 NN} \\ \tilde{s}_2, & \text{if } (i,j) \text{ is 2 NN} \\ \tilde{s}_3, & \text{if } (i,j) \text{ is 3 NN} \\ 0, & \text{else} \end{cases} \quad (13)$$

In **Table 1**, some parameter sets are presented that have shown to reliably reproduce the DFT band structure of different graphene systems.

However, while this approach is reasonable for infinite graphene sheets where electronic correlations are commonly thought to be weak, it provides insufficiently accurate results for finite graphene structures such as nanoribbons. For the latter, it

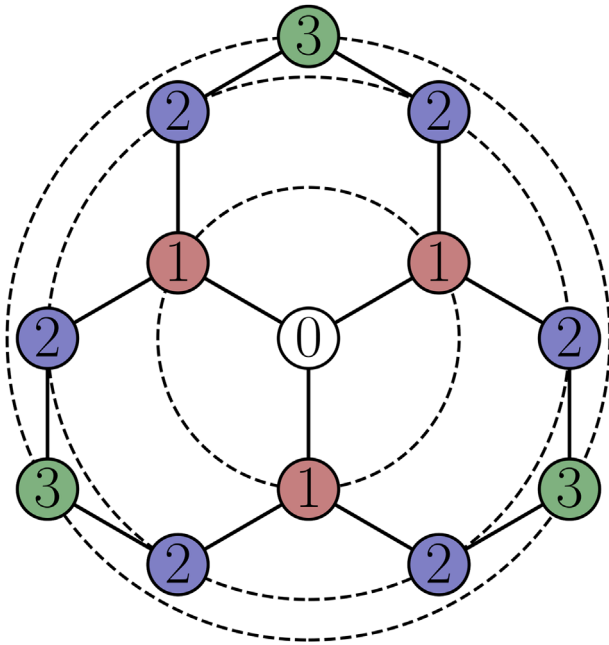


Figure 1. Illustration of the positions of neighboring sites in the graphene honeycomb lattice. The three nearest neighbors (1NN) of the white site are marked in red, the six second-nearest neighbors (2NN) in blue and the three third-nearest neighbors (3NN) in green.

is known that the reduction of screening that is due to the quantum confinement, results in stronger electron–electron correlations and the emergence of a band gap which cannot be described sufficiently well by DFT (LDA) calculations.^[12,39] Instead, it was found that including quasiparticle corrections using the G_0W_0 approximation results in a larger band gap that is in better agreement with experimental findings.^[26,40] Thus, the tight-binding approach presented above that is able to reproduce DFT band structures has to be extended to include correlations.

2.2. Extension to Hartree–Fock

In a first step electron interactions can be included on the Hartree–Fock (HF) level. Since this case can still be described by an effective single-particle Hamiltonian, only the matrix elements $\tilde{h}_{ji}^{\text{TB}}$ in Equation (6) have to be replaced by the ones of the new Hamiltonian containing mean-field interactions while the rest of the derivation in Section 2.1 remains untouched.

To derive the HF Hamiltonian it is convenient to express it in second quantization. The creation and annihilation operators obey the same transformation relation between the two basis sets as the single-particle orbitals, *cf.* Equation (8). Thus, in the nonorthogonal basis the generalized operators, *cf.* Equation (18), that create and annihilate an electron with spin σ on site i can be written as

$$\tilde{c}_{i,\sigma}^\dagger = \sum_k \hat{c}_{k,\sigma}^\dagger \tilde{S}_{ki}^\dagger \quad (14)$$

$$\tilde{c}_{i,\sigma} = \sum_k \tilde{S}_{ik}^\dagger \hat{c}_{k,\sigma} \quad (15)$$

Since the overlap matrix S is real and symmetric it follows immediately from Equations (14) and (15) that the creation and annihilation operators fulfill the known involutivity condition

$$\left(\tilde{c}_{i,\sigma}^\dagger\right)^\dagger = \tilde{c}_{i,\sigma} \quad (16)$$

Additionally, as is the case of the orthonormal basis, two creation and two annihilation operators anticommute

$$\left\{\tilde{c}_{i,\sigma}^\dagger, \tilde{c}_{i,\tau}^\dagger\right\} = \left\{\tilde{c}_{i,\sigma}, \tilde{c}_{i,\tau}\right\} = 0 \quad (17)$$

However, the anticommutation relation between a creation operator and an annihilation operator is modified and contains the overlap matrix

$$\left\{\tilde{c}_{j,\sigma}^\dagger, \tilde{c}_{i,\tau}\right\} = \delta_{\sigma\tau} \tilde{S}_{ij} \quad (18)$$

which for $\tilde{S}_{ij} = \delta_{ij}$ reduces to the familiar anticommutator in an orthonormal basis.

Table 1. Various parameter sets for the hopping (cf. Equation (12)) and overlap (cf. Equation (13)) matrix in the extended Hubbard model.

Structure	Set	J [eV]	\tilde{E}_{2p} [J]	\tilde{t}_1 [J]	\tilde{t}_2 [J]	\tilde{t}_3 [J]	\tilde{S}_1	\tilde{S}_2	\tilde{S}_3
2D Graphene	1NN	2.7	0	1	–	–	–	–	–
	3NN ^[35] (Reich2002)	2.97	0.094	1	0.025	0.111	0.073	0.018	0.026
Graphene nanoribbons	3NN ^[36] (Tran2017)	2.756	0.068	1	0.026	0.138	0.093	0.079	0.070

For homogeneous graphene the parameters are taken from Reich et al.^[35] and for GNRs from Tran et al.^[36]

The action of a creation operator $\tilde{c}_{i,\sigma}^\dagger$ and annihilation operator $\tilde{c}_{i,\sigma}$ on an arbitrary N -particle state $|\{n\}\rangle$ is defined as

$$\begin{aligned}\tilde{c}_{i,\sigma}^\dagger|\{n\}\rangle &= (1 - n_{i,\sigma})(-1)^{a_{i,\sigma}}|\{n\}^{i,\sigma}\rangle, \\ \tilde{c}_{i,\sigma}|\{n\}\rangle &= \sum_k n_{k,\sigma}(-1)^{a_{k,\sigma}}\tilde{S}_{ik}|\{n\}k,\sigma\rangle\end{aligned}\quad (19)$$

where the notation $|\{n\}^{i,\sigma}\rangle$ and $|\{n\}_{i,\sigma}\rangle$ denotes that a particle with spin σ was added or removed at site i , respectively, $n_{i,\sigma}$ is the occupation number of the orbital corresponding to site i and spin σ and $a_{k,\sigma} = \sum_{l < k} n_{l,\sigma}$.

In the basis of these canonical operators given in Equations (14) and (15), a Hamiltonian including single-particle and two-particle contributions has the form

$$\begin{aligned}\hat{H} &= \sum_{ijkl} \tilde{S}_{ik}^{-1} \tilde{h}_{kl}^{\text{TB}} \tilde{S}_{ij}^{-1} \tilde{c}_{i,\sigma}^\dagger \tilde{c}_{j,\sigma} \\ &\quad \sigma \in \{\uparrow, \downarrow\} \\ &+ \frac{1}{2} \sum_{ijklmnpq} \tilde{S}_{im}^{-1} \tilde{S}_{jn}^{-1} \tilde{w}_{mnpq}^{\sigma\tau\sigma\tau} \tilde{S}_{pk}^{-1} \tilde{S}_{ql}^{-1} \tilde{c}_{i,\sigma}^\dagger \tilde{c}_{j,\tau}^\dagger \tilde{c}_{l,\tau} \tilde{c}_{k,\sigma}\end{aligned}\quad (20)$$

where the matrix elements of the interaction $\tilde{w}_{mnpq}^{\sigma\tau\sigma\tau}$ do not allow for spin flips and the single-particle contribution $\tilde{h}_{kl}^{\text{TB}}$ is assumed to be spin independent. Further, the matrix elements of the effective single-particle Hartree–Fock Hamiltonian, the so called Fock matrix $\tilde{h}_{ij}^{\text{eff}}$, are given by^[41]

$$\tilde{h}_{ij}^{\text{eff}} = \tilde{h}_{ij}^{\text{TB}} + \sum_{klmn} \left(\tilde{w}_{imjn}^{\sigma\tau\sigma\tau} - \tilde{w}_{imnj}^{\sigma\sigma\sigma\sigma} \right) \tilde{S}_{nl}^{-1} \tilde{\rho}_{lk,\sigma} \tilde{S}_{km}^{-1}\quad (21)$$

where $\tilde{\rho}_{lk,\sigma} = \langle \tilde{c}_{k,\sigma}^\dagger \tilde{c}_{l,\sigma} \rangle$ is the element of the reduced density matrix in the nonorthogonal basis.^[42]

Inserting these matrix elements in Equation (6) for $\tilde{\mathbf{H}}$ results in the well-known Roothaan–Hall equations^[43–45]

$$\tilde{\mathbf{F}}\tilde{\mathbf{A}} = \tilde{\mathbf{S}}\tilde{\mathbf{A}}\mathbf{E}\quad (22)$$

with $\tilde{\mathbf{F}}$ containing the matrix elements $\tilde{h}_{ij}^{\text{eff}}$. Again, a Löwdin orthogonalization results in a standard eigenvalue problem in the orthonormal basis

$$\mathbf{F}\mathbf{A} = \mathbf{A}\mathbf{E},\quad (23)$$

with

$$\mathbf{F} = \tilde{\mathbf{S}}^{-\frac{1}{2}} \tilde{\mathbf{F}} \tilde{\mathbf{S}}^{-\frac{1}{2}}\quad (24)$$

Since the Fock matrix contains the elements of the density matrix, Equation (23) has to be solved self consistently until convergence is reached.

A similar approach was already successfully applied by Hancock et al.^[46] for transport calculations in graphene nanoribbons using a Hubbard type on-site interaction of the form

$$\tilde{w}_{ijkl}^{\sigma\tau\sigma\tau} = U\delta_{ij}\delta_{ik}\delta_{il}\bar{\delta}_{\sigma\tau}\quad (25)$$

where $\bar{\delta}_{\sigma\tau} = 1 - \delta_{\sigma\tau}$ enforces Pauli blocking and U is a free parameter that corresponds to the strength of the interaction. For these interaction elements the Fock matrix becomes

$$\tilde{h}_{ij}^{\text{eff}} = \tilde{h}_{ij}^{\text{TB}} + \delta_{ij}U\sum_{kl} \tilde{S}_{il}^{-1} \tilde{\rho}_{lk} \tilde{S}_{ki}^{-1}\quad (26)$$

with $\tilde{\rho}_{lk} := \tilde{\rho}_{lk,\uparrow} + \tilde{\rho}_{lk,\downarrow}$. However, as discussed in Section 2.1, a pure mean-field approach is not sufficient to correctly describe finite graphene nanosystems. For an accurate treatment one has to take into account electronic correlations. Therefore, we will extend the description systematically using the formalism of nonequilibrium Green functions (NEGF) that is described in the next section. Since it is convenient to treat the NEGF approach in an orthonormal basis, it is useful to also express the Fock matrix in this basis. Using Equations (21) and (24) results in

$$h_{ij}^{\text{eff}} = h_{ij}^{\text{TB}} + \sum_{kl} \left(w_{ikjl}^{\sigma\tau\sigma\tau} - w_{iklj}^{\sigma\sigma\sigma\sigma} \right) \rho_{lk,\sigma}\quad (27)$$

with the matrix elements in the orthonormal basis given by

$$h_{ij}^{\text{TB}} = \sum_{kl} \tilde{S}_{ik}^{-\frac{1}{2}} \tilde{h}_{kl}^{\text{TB}} \tilde{S}_{lj}^{-\frac{1}{2}}\quad (28)$$

$$\rho_{ij,\sigma} = \sum_{kl} \tilde{S}_{ik}^{-\frac{1}{2}} \tilde{\rho}_{kl,\sigma} \tilde{S}_{lj}^{-\frac{1}{2}}\quad (29)$$

$$w_{ijkl}^{\sigma\tau\sigma\tau} = \sum_{mnpq} \tilde{S}_{im}^{-\frac{1}{2}} \tilde{S}_{jn}^{-\frac{1}{2}} \tilde{w}_{mnpq}^{\sigma\tau\sigma\tau} \tilde{S}_{pk}^{-\frac{1}{2}} \tilde{S}_{ql}^{-\frac{1}{2}} \quad (30)$$

In the special case of an on-site Hubbard interaction, cf. Equation (25), the interaction elements in the orthonormal basis reduce to

$$w_{ijkl}^{\sigma\tau\sigma\tau} = U \bar{\delta}_{\sigma\tau} \sum_m \tilde{S}_{im}^{-\frac{1}{2}} \tilde{S}_{jm}^{-\frac{1}{2}} \tilde{S}_{mk}^{-\frac{1}{2}} \tilde{S}_{ml}^{-\frac{1}{2}} =: w_{ijkl} \bar{\delta}_{\sigma\tau} \quad (31)$$

Finally, the spin-resolved Fock matrix is then given by

$$h_{ij,\uparrow(\downarrow)}^{\text{eff}} = h_{ij}^{\text{TB}} + \sum_{kl} w_{ikjl} \rho_{lk,\downarrow(\uparrow)} \quad (32)$$

which will later on be used in the propagation of the nonequilibrium Green functions, see Section 3.1.

3. Nonequilibrium Green Functions Approach

The single-particle Green function G is the central property in the nonequilibrium Green functions approach. It is defined on the Keldysh time contour C as^[47,48]

$$G_{ij}^{\sigma}(z, z') = -\frac{i}{\hbar} \langle T_C \hat{c}_{i,\sigma}(z) \hat{c}_{j,\sigma}^{\dagger}(z') \rangle \quad (33)$$

where $\langle \dots \rangle$ is the ensemble average and the creation and annihilation operator are defined in an orthonormal basis. Due to the spin symmetry of the considered systems the spin indices will be neglected in the further discussion and the Green function will be simplified to^[49]

$$G_{ij}(z, z') := G_{ij}^{\uparrow}(z, z') = G_{ij}^{\downarrow}(z, z') \quad (34)$$

In order to make the complex-time Green function numerically accessible, it is useful to define real-time contour components of the Green function based in the relative positions of the complex times z and z' on the contour, namely the less ($G^<$), greater ($G^>$), retarded (G^R), and advanced (G^A) component that are defined as

$$G_{ij}^<(t, t') = -\frac{1}{i\hbar} \langle \hat{c}_j^{\dagger}(t') \hat{c}_i(t) \rangle \quad (35)$$

$$G_{ij}^>(t, t') = \frac{1}{i\hbar} \langle \hat{c}_i(t) \hat{c}_j^{\dagger}(t') \rangle \quad (36)$$

$$G_{ij}^R(t, t') = \Theta(t, t') \left(G_{ij}^>(t, t') - G_{ij}^<(t, t') \right) \quad (37)$$

$$G_{ij}^A(t, t') = \Theta(t', t) \left(G_{ij}^<(t, t') - G_{ij}^>(t, t') \right) \quad (38)$$

where $\Theta(t, t')$ denotes the Heaviside step function.

As a generalization of the single-particle density matrix, $\rho_{ij} = \langle \hat{c}_j^{\dagger} \hat{c}_i \rangle$, onto the two-time plane the Green function carries all information about the single-particle density on the time diagonal

$$\rho_{ij}(t) = -i\hbar G_{ij}^<(t, t) \quad (39)$$

With this, one gets access to the time-dependent expectation value of any single-particle operator \hat{A}_1 , such as the single-particle energy, via

$$\langle \hat{A}_1 \rangle(t) = -i\hbar \sum_{ij} A_{ij} G_{ji}^<(t, t) \quad (40)$$

One should note that when combined with the TB approach presented in Section 2.1 the orthonormal basis of the Green function does not correspond to the nonorthogonal basis of the $2p_z$ atomic orbitals of the carbon lattice. For the density matrix the transformation to the physical basis can be performed by the inverse of Equation (29) which leads to

$$\tilde{\rho}_{ij} = \sum_{kl} \tilde{S}_{ik}^{-\frac{1}{2}} \rho_{kl} \tilde{S}_{lj}^{\frac{1}{2}} \quad (41)$$

In this basis the occupation on a single lattice site i is then given by

$$\langle \hat{\rho}_{ii} \rangle = \sum_k \tilde{S}_{ik}^{-1} \tilde{\rho}_{ki} \quad (42)$$

Since the Green function is defined as a two-time quantity (cf. Equation (33)), it also gives access to the spectral properties of the system. The local spectral function is given by a Fourier transform with respect to the relative time,

$$A_i(\omega) = i\hbar \int dt dt' e^{-i\omega(t-t')} [G_{ii}^>(t, t') - G_{ii}^<(t, t')] \quad (43)$$

The sum over all local contributions of the spectral function results in the density of states (DOS) of the system. Combining the temporal transform in Equation (43) with a spatial one results in an expression for the full energy dispersion relation

$$A(\omega, k) = \frac{i\hbar}{N_s} \sum_{ij} e^{-ik(i-j)} \int dt dt' e^{-i\omega(t-t')} \times [G_{ij}^>(t, t') - G_{ij}^<(t, t')] \quad (44)$$

Another important quantity is the time-resolved photoemission spectrum^[50,51]

$$A^<(\omega, T) = -i\hbar \sum_i \int dt dt' S_{\kappa}(t-T) S_{\kappa}(t'-T) \times e^{-i\omega(t-t')} G_{ii}^<(t, t') \quad (45)$$

as it allows for direct comparison with photoemission experiments. Here, S is a Gaussian function to simulate the probe pulse that is used in corresponding experiments

$$S_{\kappa}(t) = \frac{1}{\kappa\sqrt{2\pi}} \exp\left(-\frac{t^2}{2\kappa^2}\right) \quad (46)$$

with a given pulse width κ .

3.1. Equations of Motion

The time evolution of the Green function on the Keldysh contour is given by the Kadanoff–Baym equations (KBEs),^[52]

$$\begin{aligned} \sum_I \left[i\hbar \frac{d}{dz} \delta_{il} - h_{il}^{\text{TB}}(z) \right] G_{ij}(z, z') \\ = \delta_{ij} \delta_C(z, z') + \sum_I \int_C d\bar{z} \Sigma_{il}(z, \bar{z}) G_{ij}(\bar{z}, z') \end{aligned} \quad (47)$$

and the adjoint equation. The KBEs would be formally exact if the self-energy Σ in the collision integral on the right hand side of the equation was known. However, for most system the exact self-energy is not accessible. Hence, approximations to the NEGF scheme are introduced via proper choices of the self-energy. A more detailed discussion on the approximations used here is given in Section 3.2. The self-energy can be separated into a time-diagonal mean-field contribution and a correlation part

$$\Sigma(z, z') = \delta_C(z, z') \Sigma^{\text{HF}}(z) + \Sigma^{\text{corr}}(z, z') \quad (48)$$

Due to the contour delta distribution $\delta_C(z, z')$ the Hartree–Fock part of the self-energy can be included into the Hamiltonian on the left side of Equation (47) resulting in an effective single-particle Hamiltonian that is equivalent to the Fock matrix in Equation (27). Now the KBE can be written as

$$\begin{aligned} \sum_I \left[i\hbar \frac{d}{dz} \delta_{il} - h_{il}^{\text{eff}}(z) \right] G_{ij}(z, z') \\ = \delta_{ij} \delta_C(z, z') + \sum_I \int_C d\bar{z} \Sigma_{il}(z, \bar{z}) G_{ij}(\bar{z}, z') \end{aligned} \quad (49)$$

where the self-energy $\Sigma(t, t') := \Sigma^{\text{corr}}(t, t')$ only contains the correlation part.

In practice, the KBEs are solved for the less and greater real-time components of the Green function. In order to get access to the full single-particle information of the system, it is necessary to obtain $G^>(t, t')$ and $G^<(t, t')$ in the complete (t, t') -plane. However, due to the symmetry relation $G_{ij}^<(t, t') = -[G_{ji}^>(t', t)]^*$ each of the two KBEs (Equation (49) and the adjoint) has to be solved for only one real-time argument and component of the Green function. One possible choice of equations is:

$$\sum_I \left[i\hbar \frac{d}{dt} \delta_{il} - h_{il}^{\text{eff}}(t) \right] G_{ij}^>(t, t') = I_{ij}^{(1),>}(t, t') \quad (50)$$

$$\sum_I G_{il}^<(t, t') \left[-i\hbar \frac{d}{dt'} \delta_{il} - h_{ij}^{\text{eff}}(t') \right] = I_{ij}^{(2),<}(t, t') \quad (51)$$

where on the right-hand side the collision integrals $I^{(1),>}$ and $I^{(2),<}$ are introduced. They are defined as

$$I_{ij}^{(1),>}(t, t') := \sum_I \int_{t_s}^{\infty} d\bar{t} \left\{ \Sigma_{il}^{\text{R}}(t, \bar{t}) G_{ij}^>(\bar{t}, t') + \Sigma_{il}^>(t, \bar{t}) G_{ij}^{\text{A}}(\bar{t}, t') \right\} \quad (52)$$

$$I_{ij}^{(2),<}(t, t') := \sum_I \int_{t_s}^{\infty} d\bar{t} \left\{ G_{il}^{\text{R}}(t, \bar{t}) \Sigma_{ij}^<(\bar{t}, t') + G_{il}^<(t, \bar{t}) \Sigma_{ij}^{\text{A}}(\bar{t}, t') \right\} \quad (53)$$

with the starting time t_s , see Section 3.3 for a discussion. This way, $G^<(t, t')$ is propagated above and $G^>(t, t')$ below the time diagonal. For $t = t'$ either one of them can be calculated while the other one can be accessed by the symmetry relation on the time diagonal

$$G_{ij}^>(t, t) - G_{ij}^<(t, t) = -\frac{i}{\hbar} \delta_{ij} \quad (54)$$

Likewise, the collision integrals $I^{(1),>}(t, t')$ and $I^{(2),<}(t, t')$ have to be calculated for times $t > t'$ and $t < t'$ only, respectively. To this end a new notation is introduced for a general contour quantity A ,

$$A(t \gtrless t') := A(t, t')|_{i \gtrless t'} \quad (55)$$

This results in three equations of motion for the full two-time propagation of the real-time components of the Green function:

$$\begin{aligned} i\hbar \frac{d}{dt} G_{ij}^>(t \geq t') = \sum_I h_{il}^{\text{eff}}(t) G_{il}^>(t \geq t') \\ + I_{ij}^{(1),>}(t \geq t') \end{aligned} \quad (56)$$

$$\begin{aligned} -i\hbar \frac{d}{dt'} G_{ij}^<(t \leq t') = \sum_I G_{il}^<(t \leq t') h_{ij}^{\text{eff}}(t') \\ + I_{ij}^{(2),<}(t \leq t') \end{aligned} \quad (57)$$

$$\begin{aligned} i\hbar \frac{d}{dt} G_{ij}^<(t, t) = \left[h^{\text{eff}}(t), G^<(t, t) \right]_{ij} \\ + I_{ij}^{(1),>}(t, t) - I_{ij}^{(2),<}(t, t) \end{aligned} \quad (58)$$

In order to solve these equations of motion, the collision integrals that appear in Equations (56)–(58) have to be expressed in terms of $G^<(t < t')$ and $G^>(t > t')$. Using the definition of the advanced and retarded Green function and self-energy (cf. Equations (37) and (38)) one arrives, after some calculations, at the following expressions for the collision integrals at a given time step T :

$$\begin{aligned}
 I_{ij}^{(1),>}(T > t') &= \int_{t_s}^{t'} d\bar{t} \sum_k \left\{ \Sigma_{ik}^>(T > \bar{t}) G_{kj}^<(\bar{t} < t') \right. \\
 &\quad \left. - \left(\Sigma_{ki}^<(\bar{t} < T) G_{jk}^>(t' > \bar{t}) \right)^* \right\} \\
 &\quad + \int_{t'}^T d\bar{t} \sum_k \left\{ \Sigma_{ik}^>(T > \bar{t}) G_{kj}^>(\bar{t} > t') \right. \\
 &\quad \left. + \left(\Sigma_{ki}^<(\bar{t} < T) \right)^* G_{jk}^>(\bar{t} > t') \right\} \quad (59)
 \end{aligned}$$

$$\begin{aligned}
 I_{ij}^{(2),<}(t < T) &= \int_{t_s}^t d\bar{t} \sum_k \left\{ G_{ik}^>(t > \bar{t}) \Sigma_{kj}^<(\bar{t} < T) \right. \\
 &\quad \left. - \left(G_{ki}^<(\bar{t} < t) \Sigma_{jk}^>(T > \bar{t}) \right)^* \right\} \\
 &\quad + \int_t^T d\bar{t} \sum_k \left\{ G_{ik}^<(t < \bar{t}) \Sigma_{kj}^<(\bar{t} < T) \right. \\
 &\quad \left. + G_{ik}^<(t < \bar{t}) \left(\Sigma_{jk}^>(T > \bar{t}) \right)^* \right\} \quad (60)
 \end{aligned}$$

for the off-diagonal elements and

$$\begin{aligned}
 I_{ij}^{(1),>}(T, T) &= \int_{t_s}^T d\bar{t} \sum_k \left\{ \Sigma_{ik}^>(T > \bar{t}) G_{kj}^<(\bar{t} < T) \right. \\
 &\quad \left. - \left(\Sigma_{ki}^<(\bar{t} < T) G_{jk}^>(T > \bar{t}) \right)^* \right\} \quad (61)
 \end{aligned}$$

$$\begin{aligned}
 I_{ij}^{(2),<}(T, T) &= \int_{t_s}^T d\bar{t} \sum_k \left\{ G_{ik}^>(T > \bar{t}) \Sigma_{kj}^<(\bar{t} < T) \right. \\
 &\quad \left. - \left(G_{ki}^<(\bar{t} < T) \Sigma_{jk}^>(T > \bar{t}) \right)^* \right\} \\
 &= - \left(I_{ji}^{(1),>}(T, T) \right)^* \quad (62)
 \end{aligned}$$

for the time diagonal. These equations do only depend on $G^<(t < t')$, $G^>(t > t')$, $\Sigma^<(t < t')$, and $\Sigma^>(t > t')$. Therefore, if it is possible to express the self-energy in terms of the less and greater components of the Green function – which is possible for all relevant approximations, cf. Section 3.2 – the propagation scheme will be closed. Examples for application of this NEGF scheme to Hubbard clusters can be found for example, in refs. [32,53–55]. Computational details will be presented in Section 3.3.

3.2. Self-Energy Approximations

The exact self-energy Σ contains the full N -particle information of the system. However, since in most cases the exact solution is not known one has to develop many-body approximations (MBA) to the self-energy. For this, as shown in Equation (48),

the self-energy can be separated into a Hartree–Fock and a correlation contribution. The time-diagonal mean-field part can be included in an effective single-particle Hamiltonian and the remaining self-energy contains only the correlation part, cf. Equation (49).

The mean-field Hamiltonian was derived in Section 2.2 and its elements are given by the Fock matrix, cf. Equation (32). For a Hubbard-type on-site interaction that is considered here, the matrix elements of the interaction in the orthonormal basis are defined in Equation (31). The corresponding diagram is depicted in **Figure 2**. Due to the spin delta $\delta_{\sigma\tau}$ the exchange contribution vanishes and only the direct mean-field diagram remains.

While in the nonorthogonal basis the strength of the on-site interaction is defined by the parameter U , in the orthonormal basis this leads to a local interaction, cf. Equation (31)

$$w_{ijkl} = U \sum_m \tilde{S}_{im}^{-\frac{1}{2}} \tilde{S}_{jm}^{-\frac{1}{2}} \tilde{S}_{mk}^{-\frac{1}{2}} \tilde{S}_{ml}^{-\frac{1}{2}} \quad (63)$$

For higher-order approximations to the correlation self-energy this would result in a high numerical complexity. In order to reduce the numerical effort, here, only the diagonal contribution to the interaction

$$U_i := w_{iiii} U \sum_m \tilde{S}_{im}^{-\frac{1}{2}} \tilde{S}_{im}^{-\frac{1}{2}} \tilde{S}_{mi}^{-\frac{1}{2}} \tilde{S}_{mi}^{-\frac{1}{2}} \quad (64)$$

is taken into account. This approximation is valid if the overlap matrix \tilde{S} – and consequently $\tilde{S}^{-\frac{1}{2}}$ – has mainly diagonal contributions which is the case for the considered parameter set, cf. Table 1 and Equation (13). Further, it allows for a fast calculation of higher-order self-energy contributions. The two approximations specifically used in this work are presented in the following using a generalized time-dependent $U(t)$ for the adiabatic switching procedure, cf. Section 3.3.

The second-Born (2B) approximation is the most simple approach to add correlations to the self-energy. The idea is to describe the scattering event between two particles by considering only the first term in the Born series.^[47] This results in the following expression for the 2B self-energy

$$\Sigma_{ij}^{2B,>}(T > t') = \hbar^2 U_i(T) U_j(t') G_{ij}^>(T > t') G_{ij}^>(T > t') G_{ji}^<(t' < T) \quad (65)$$

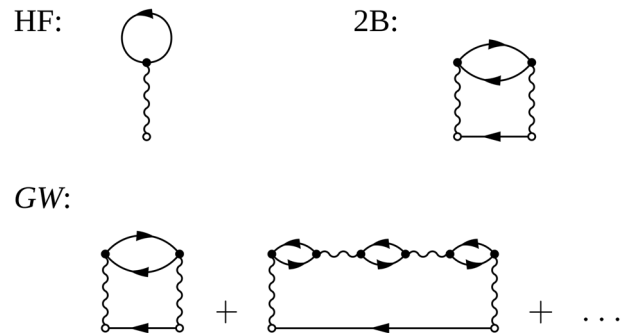


Figure 2. Feynman diagrams for the self-energy approximations used in this work: Hartree–Fock (HF), second-order Born approximation (2B), and Hedin's GW approximation.

$$\Sigma_{ij}^{2B,<}(t < T) = \hbar^2 U_i(t) U_j(T) G_{ij}^{<}(t < T) G_{ij}^{<}(t < T) G_{ij}^{>}(T > t) \quad (66)$$

It includes all terms up to second order in the interaction U but no higher-order terms. Thus, it is a reasonable approach when the interaction strength is low. From a numerical point of view the 2B self-energy is easy to calculate since no integration over a time argument has to be performed. A diagrammatic representation is shown in Figure 2. More details can be found in refs. [47,56,57].

The GW approximation is a more sophisticated approach that takes the dynamically screened interaction between particles into account. The real-time components of the self-energy are given by

$$\Sigma_{ij}^{GW,>}(T > t') = i\hbar W_{ji}^{<,\uparrow\uparrow}(t' < T) G_{ij}^{>}(T > t') \quad (67)$$

$$\Sigma_{ij}^{GW,<}(t < T) = i\hbar W_{ij}^{<,\uparrow\uparrow}(t < T) G_{ij}^{<}(t < T) \quad (68)$$

The less component of the same-spin screened interaction $W^{<,\uparrow\uparrow}$ has to be calculated in an iterative manner. For this, it is convenient to define the retarded and advanced component of the two-particle Fock-like Green function

$$G_{ij}^{F,R}(t > t') = G_{ij}^{>}(t > t') G_{ji}^{<}(t' < t) - \left(G_{ji}^{<}(t' < t) \right)^* \left(G_{ij}^{>}(t > t') \right)^* \quad (69)$$

$$G_{ij}^{F,A}(t < t') = G_{ij}^{<}(t < t') G_{ji}^{>}(t' > t) - \left(G_{ji}^{>}(t' > t) \right)^* \left(G_{ij}^{<}(t < t') \right)^* \quad (70)$$

Now, the same-spin screened interaction is given by

$$\begin{aligned} W_{ij}^{<,\uparrow\uparrow}(t < T) = & -i\hbar U_i(t) G_{ij}^{F,<}(t < T) U_j(T) \\ & -i\hbar U_i(t) \sum_k \int_{t_s}^t d\bar{t} G_{ik}^{F,R}(t > \bar{t}) W_{kj}^{<,\uparrow\uparrow}(\bar{t} < T) \\ & -i\hbar U_i(t) \sum_k \int_{t_s}^t d\bar{t} \left(G_{ki}^{F,<}(\bar{t} < t) \right)^* W_{kj}^{A,\uparrow\uparrow}(\bar{t} < T) \\ & -i\hbar U_i(t) \sum_k \int_t^T d\bar{t} G_{ik}^{F,<}(t < \bar{t}) W_{kj}^{A,\uparrow\uparrow}(\bar{t} < T) \end{aligned} \quad (71)$$

It depends on the different-spin screened interaction

$$\begin{aligned} W_{ij}^{<,\uparrow\downarrow}(t < T) = & -i\hbar U_i(t) G_{ij}^{F,<}(t < T) U_j(T) \\ & -i\hbar U_i(t) \sum_k \int_{t_s}^t d\bar{t} G_{ik}^{F,R}(t > \bar{t}) W_{kj}^{<,\uparrow\downarrow}(\bar{t} < T) \\ & -i\hbar U_i(t) \sum_k \int_{t_s}^t d\bar{t} \left(G_{ki}^{F,<}(\bar{t} < t) \right)^* W_{kj}^{A,\uparrow\downarrow}(\bar{t} < T) \\ & -i\hbar U_i(t) \sum_k \int_t^T d\bar{t} G_{ik}^{F,<}(t < \bar{t}) W_{kj}^{A,\uparrow\downarrow}(\bar{t} < T) \end{aligned} \quad (72)$$

that, again, contains the same-spin screened interaction $W^{<,\uparrow\downarrow}$. Additionally, these two coupled equations depend on the advanced components of the same- and different-spin screened interaction that are given by

$$\begin{aligned} W_{ij}^{A,\uparrow\downarrow}(t < T) = & -i\hbar U_i(t) G_{ij}^{F,A}(t < T) U_j(T) \\ & +i\hbar U_i(t) \sum_k \int_t^T d\bar{t} G_{ik}^{F,A}(t < \bar{t}) W_{kj}^{A,\uparrow\downarrow}(\bar{t} < T) \end{aligned} \quad (73)$$

$$W_{ij}^{A,\uparrow\uparrow}(t < T) = i\hbar U_i(t) \sum_k \int_t^T d\bar{t} G_{ik}^{F,A}(t < \bar{t}) W_{kj}^{A,\uparrow\uparrow}(\bar{t} < T) \quad (74)$$

In order to solve this system of coupled equations numerically, first, the two advanced components of the screened interaction are calculated. On the time diagonal a solution can be immediately found for both:

$$W_{ij}^{A,\uparrow\downarrow}(T, T) = -i\hbar U_i(T) G_{ij}^{F,A}(T, T) U_j(T) \quad (75)$$

$$W_{ij}^{A,\uparrow\uparrow}(T, T) = 0 \quad (76)$$

Next, Equations (73) and (74) can be solved simultaneously in an iterative manner for every time t starting from the diagonal. After that, Equations (71) and (72) are iterated until convergence for every time step t , this time starting at t_s . This way, the less and greater component of the GW self-energy can be computed according to Equations (67) and (68).

Due to its integral (Dyson) equation structure the GW approach contains contributions up to infinite order in U . Therefore, it is much more challenging than the 2B approximation, from a numerical perspective. But this effort is warranted because the GW approximation has shown very good results for systems near half filling, where screening effects are important.^[58] Furthermore, it is frequently used for band structure and photoemission calculations.^[59,60] The first three diagrams of the GW approximation are depicted in Figure 3. A detailed derivation of these equations and the corresponding expressions for other self-energies can be found in ref. [61].

With the self-energies given in Equations (65)–(68) the propagation scheme for the real-time components of the Green function is closed.

3.3. Numerical Solution of the Keldysh–Kadanoff–Baym Equations for GNR

Despite the application of the diagonal Hubbard interaction the numerical solution of the KBEs remains a challenging task. For a given time step T , first, the effective single-particle Hamiltonian h_{ij}^{eff} (cf. Equation (32)) and the chosen self-energy (cf. Equations (65)–(68)) have to be calculated from the Green functions. Now all quantities are known that are needed to determine the collision integrals $I^{(1),>}$ and $I^{(2),<}$ via Equations (59)–(62). Next, the components of the Green function can be propagated one

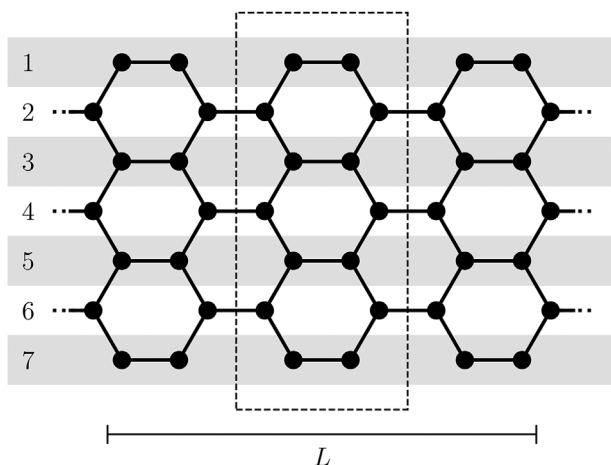


Figure 3. Illustration of the structure of an armchair graphene nanoribbon (AGNR). The width $N (= 7)$ and the length $L (= 7)$ of the graphene ribbon is defined as the number of dimer and zigzag lines of carbon atoms, respectively. Here, a 7-AGNR is shown. The dashed rectangle defines the unit cell of the ribbon. In Figure 1 the positions of the nearest neighbors in a GNR are depicted.

time step further to $T + \Delta$ using Equations (56)–(58), where Δ is the time step size. Before the actual propagation is started the ground state of the system has to be calculated, which is done via adiabatic switching. A detailed description of this procedure is given in ref. [32]. An alternative procedure to obtain the ground state is the inclusion of the imaginary-time branch in the Keldysh time contour.^[47,62] Both methods have their advantages, adiabatic switching results in additional propagation time while the imaginary branch leads to the occurrence of extra terms in the collision integrals.^[63]

Since the calculation of the self-energies and collision integrals require the Green function on the complete two-time plane, the computational memory demand and calculation time of the propagation algorithm show a quadratic and cubic scaling, respectively, with respect to both, the basis size and the number of time steps.

In order to nevertheless keep the numerical challenges in check a lot of sophisticated improvements have been made to the propagation techniques of the NEGF scheme. For the solution of the KBEs a fourth-order Runge–Kutta method is used while the time integrals occurring in the calculation of the self-energies and the collision integrals are determined using high-order Newton–Cotes and Fourier extension algorithms.

From a performance perspective, another crucial part of the propagation scheme is the huge number of matrix multiplications which can be parallelized with respect to the spatial and temporal indices. In theory, this can be utilized to massively speed-up the simulation on an appropriate architecture. Therefore, all calculations in this work have been performed using graphics processing units (GPUs) that are known to greatly outperform CPUs when it comes to parallel calculations.^[64]

In the past, our NEGF simulations have been carefully tested for convergence with respect to the time step where, among others, particle number and total energy conservation are monitored, for example, Ref. [31], and also time reversibility^[65,66] is verified. For small systems tests against exact diagonalization

calculations are performed. Additionally, comparisons with 2D cold atom experiments^[32,67] and 1D density-matrix renormalization group (DMRG) calculations^[30] showed excellent accuracy of our simulations.

4. Results

The system of interest in this paper are so-called graphene nanoribbons (GNR) which are quasi-one-dimensional slices of graphene. Because of their typical width of only a few nanometers they exhibit various remarkable properties such as enhanced electron correlations due to quantum confinement effects.^[39]

The electronic properties and especially the low energy spectrum of the π -electrons is strongly influenced by the edge structure of the nanoribbons. Depending on the shape of the edges one distinguishes between armchair (AGNR) and zigzag graphene nanoribbons (ZGNR). While the model presented in Sections 2 and 3 is applicable to both types of nanoribbons, here we will focus our attention on hydrogen-passivated AGNRs. The width N of the ribbons is defined as the number of dimer lines while the length L is given by the number of zigzag lines as illustrated in Figure 3.

4.1. Ground-State Results: Band Gap, Dispersion, and Spectral Function

The extended Hubbard model introduced in Sections 2 and 3 contains eight free parameters. For the seven tight-binding parameters we choose the set proposed by Tran et al.^[36], cf. Table 1, that has been created to accurately reproduce the LDA band structure for a wide range of GNRs including different edge structures and various widths. The final free parameter of the model, the on-site interaction U , has to be adjusted to best reproduce the band structure and band gap of GNRs observed in experiments and theory that goes beyond LDA by including quasiparticle corrections. A convenient choice for the system for which the value of U can be fit is the GNR with an armchair edge and a width of seven dimer lines (7-AGNR) which is depicted in **Figure 4**. On the one hand this system has a small width which reduces the numerical effort of our calculations and, on the other hand, its ground-state properties such as the band structure and band gap have been explored in detail both theoretically and experimentally.^[12,26,68–70]

However, most experiments and theoretical works study long 7-AGNRs the band gaps of which are converged toward the value of the respective GNR for $L \rightarrow \infty$. Since our calculations are for ribbons of finite length L we have to consider the influence of finite-size effects on our results before comparing with theoretical and experimental values for the band gap. For this reason in Figure 4, we plot the size of the band gap E_g for 7-AGNRs of different lengths L within our model with the interaction set to $U = 0$ which is equivalent to the extended tight-binding model. The high numerical costs allow for calculations up to a length of $L = 16$ which corresponds to a basis size of $N_s = 112$. The band gap is given by calculating the energy dispersion, cf. Equation (44), and determining the difference

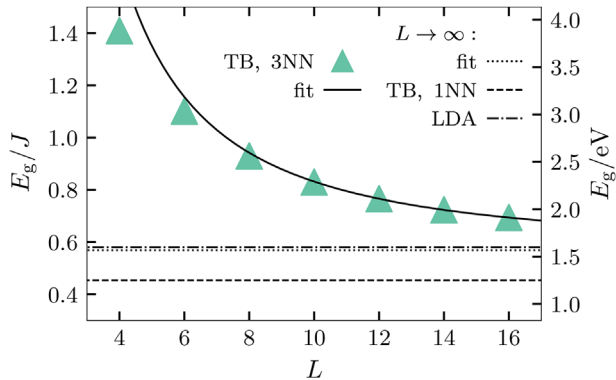


Figure 4. Band gap E_g for 7-AGNRs of different length L . The results of our model for $U = 0$ are shown as triangles. The black solid line corresponds to an exponential fit through the data points for $L = 10, \dots, 16$ and its asymptotic value for $L \rightarrow \infty$ is marked by the dotted line. As a comparison the band gap for an infinite 7-AGNR predicted by the nearest-neighbor tight-binding model and LDA are shown as dashed lines.^[68]

between the lowest peak in the upper subband and the highest peak in the lower subband at the high symmetry point K in the first Brillouin zone of graphene.

Since the band gap of the shorter ribbons $L = 4, \dots, 8$ is highly modified due to finite-size effects we perform an exponential fit through the data of the longer ribbons $L = 10, \dots, 16$ which is shown as the solid black line in Figure 4. The value of the fit for $L \rightarrow \infty$ is shown as dotted line and shows excellent agreement with the LDA gap of ≈ 1.6 eV for the 7-AGNR with infinite length. This is not surprising since the parameter set used was fit to match the LDA band structure of GNRs. As a comparison, the band gap predicted by the tight-binding model considering only nearest-neighbor hopping is considerably smaller with $E_g = 1.25$ eV. In the following, we adjust the value of U for a system of length $L = 16$. For this size the deviation of the band gap compared to the infinite system is about $0.1J$. Thus, when comparing our results for $U > 0$ we expect the observed gap to be $\approx 0.1J$ larger due to finite-size effects than it would be for an infinite ribbon.

In order to obtain a reasonable value for the interaction U , in **Figure 5** we compare the band gap of our HF, 2B and GW calculations using $U = 0, \dots, 3.5J$ for a 7-AGNR of length $L = 16$ against various theoretical and experimental results for similar 7-AGNRs in the form of horizontal lines. As already mentioned, these reference data describe the converged band gap for long ribbons ($L \rightarrow \infty$) on top of different interacting substrates.

Setting $U = 0$ the HF, 2B and GW self-energies produce the same band gap of $E_g \approx 0.7J$ which is equal to the data of Figure 4 for $L = 16$. As a result it is roughly $0.1J$ above the LDA result for free-standing ribbons with $L \rightarrow \infty$ due to finite-size effects as established in Figure 4. For HF the band gap is nearly independent of U and only slightly decreases by $\approx 0.025J$ from $U = 0$ to $U = 3.5J$. The 2B self-energy on the other hand shows an opening of the band gap starting at $U \approx 2J$ which results in a band gap at $U = 3.5J$ that is about $0.02J$ larger than for $U = 0$. Using the GW self-energy the band gap also starts to open at $U \approx 2J$. However, at $U = 3.5J$ the gap already has a size of $\approx 1J$, which is an increase of $0.3J$ compared to $U = 0$. A similar

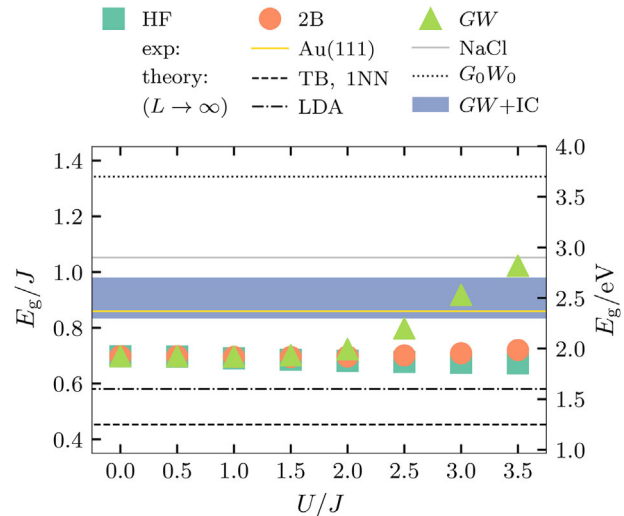


Figure 5. Band gap E_g of 7-AGNRs with a length of $L = 16$ within the extended Hubbard model using the HF (teal squares), 2B (orange circles), and GW (green triangles) self-energy as a function of the on-site interaction U . As a reference various theoretical and experimental band gaps for infinite 7-AGNRs are added. The results for free-standing GNRs are marked by dashed lines for the nearest-neighbor tight-binding model and LDA,^[68] and by a dotted line for G_0W_0 .^[12] The blue rectangle shows the area considering image-charge corrections^[69] and the gold and gray solid lines correspond to measurements for GNRs on Au(111)^[70] and NaCl,^[26] respectively.

dependence of the band gap on the on-site interaction has been observed for the one-dimensional Hubbard chain.^[71] However, here the band gap increase due to correlations in the case of 2B and GW is not as strong as in the 1D case. This is likely due to the larger bandwidth of the graphene honeycomb lattice ($6J$) compared to the one-dimensional chain lattice ($4J$) which is why an interaction of $U = 3.5J$ is less significant in the former case than in the latter.

In order to assess the quality of our results for the size of the band gap we compare to various reference data in Figure 5. While LDA calculations produce good results for weakly correlated homogeneous graphene,^[72] for graphene nanoribbons it was found that electronic correlation effects are more important and that quasiparticle corrections (G_0W_0) to LDA greatly increase the band gap to $E_g = 3.7$ eV.^[12] However, in the presence of a substrate that influences the band structure of the ribbons through screening effects smaller band gaps are observed. Measurements of 7-AGNRs on a Au(111) and NaCl surface revealed a band gap of $E_g = 2.37$ eV and $E_g = 2.9$ eV, respectively, which are between the prediction of LDA and G_0W_0 .^[26,70] Taking into account screening effects theoretically through image-charge corrections ($GW + IC$) leads to a reduced band gap of $E_g = 2.3 - 2.7$ eV compared to G_0W_0 .^[69]

Considering finite-size effects the GW self-energy for an interaction strength of $U = 3.5J$ nicely reproduces the band gap found including image-charge corrections ($GW + IC$) and measured for 7-AGNRs on Au(111).

To highlight the influence of the interaction U in the left two panels of **Figure 6**, we show the band structure (cf. Equation (44) for the energy dispersion) of the 7-AGNR of length $L = 16$

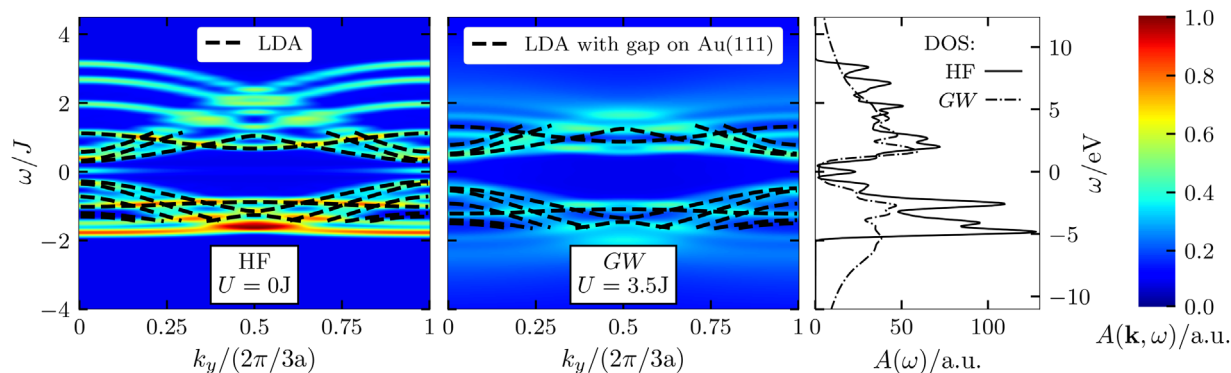


Figure 6. The left and middle panel show the energy dispersion of a 7-AGNR with a length of $L = 16$. The colormap corresponds to NEGF calculations using the HF (left) and GW (middle) self-energy with $U = 0$ and $U = 3.5J$, respectively. The dashed black lines mark the LDA band structure with the original LDA band gap (left)^[26] and shifted to obtain the band gap measured for 7-AGNRs on Au(111) (middle).^[70] The right panel shows the DOS for the NEGF results.

considered in Figure 5 for a HF calculation with $U = 0$ and a GW calculation using $U = 3.5J$. In the right panel, we plot the corresponding DOS, cf. Equation (43). The HF result is compared to the LDA band structure marked by the dashed black lines. As expected they match up nicely with some small deviations due to finite-size effects, one of them is the peak at $\omega = 0J$ which was found to vanish for $L \rightarrow \infty$. In the middle panel the dashed lines again show the LDA band structure, but shifted in such a way that the band gap corresponds to the experimental result of $E_g = 2.37$ eV for 7-AGNRs on Au(111). As found in Figure 5, the GW self-energy with $U = 3.5J$ nicely reproduces the band gap. Thus, in the vicinity of the band gap the shifted LDA result agrees with the GW band structure. However, the higher energy regions are strongly affected by correlation effects which is especially noticeable in the DOS where satellites appear for $\omega < -2J$ and $\omega > 3J$ which is outside the scope of the LDA. Therefore, the shifted LDA band structure is not accurate outside of the direct vicinity of the band gap.

In conclusion, we choose $U = 3.5J$ for the on-site interaction of the extended Hubbard model. It should be mentioned that despite only fit to 7-AGNRs, the model presented here is able to accurately describe a broad range of AGNRs. On the one hand, the set of TB parameters by Tran et al.^[36] was created to perform well for all kinds of nanoribbons with different width and edge structure and, on the other hand, it was found by Yang et al.^[12] that the influence of quasiparticle corrections results in a similar increase of the band gap compared to LDA calculations for all small AGNRs. Thus, the introduced parameter set combined with an on-site interaction of $U = 3.5J$ should be applicable to a broad range of AGNRs. Of course the value of U can be changed and determined in similar fashion if other geometries or edge shapes are to be described.

4.2. Laser-Pulse-Excited Electron Dynamics in GNR

In the following we evaluate the performance of the different self-energy approximations in the non-equilibrium regime using a 5-AGNR with a length of $L = 6$. Nanoribbons of this type and size can be produced through bottom-up synthesis.^[17] The system starts in the ground state and is subsequently excited by a

laser pulse of the form

$$E_{\text{laser}}(t) = E_0 \cos[\omega_0(t - t_0)]e^{-\frac{(t-t_0)^2}{2\sigma^2}} \quad (77)$$

with a laser amplitude of $E_0 = 0.1Je^{-1}a^{-1}$, where e is the elementary charge and $a = 0.142$ nm is the lattice constant of the system. Furthermore, a laser frequency of $\omega_0 = 2J$ is used and the standard deviation of the Gaussian is set to $\sigma = 4.35J^{-1}$. The shape of the laser pulse at $t_0 = 0$ is depicted as a solid black line in the upper panel of Figure 7. The laser excitation is treated within the dipole approximation resulting in a single-particle excitation

$$f_i(t) = -\mathbf{r}_i \cdot e\mathbf{E}_{\text{laser}}(t) \quad (78)$$

which is justified because the wavelength $\lambda_0 = 224.9$ nm of the laser pulse is a lot larger than the size $l \approx 1$ nm of the system. The excitation enters in Equation (11) as an additional time-dependent local on-site energy. In the following the direction of the electric field is set to be parallel to the armchair edge of the ribbons.

In order to study the response of the nanocluster to the laser excitation, we consider the time- and energy-resolved occupation of carriers in the conduction band. For that reason, we determine the time-dependent photoemission spectrum, cf. Equation (45), using a probe pulse width of $\kappa = 2.5J^{-1}$ at four different times, $tJ = -30, 0, 20, 50$, that are sketched in the upper panel of Figure 7 by the Gaussians of different colors. The different snapshots show the system in the ground state, during the laser interaction, directly after the laser pulse decayed and long after the laser excitation (≈ 12 fs), respectively.

In the lower panel of Figure 7, the photoemission spectrum around the Fermi energy $\omega_F = 0$ is depicted for all four times for the HF, 2B, and GW self-energies. In the ground state only states below the Fermi energy are occupied. The small spectral weight above $\omega = 0$ is due to the broadening of the highest occupied state in the valence band ($\omega < 0$) because of the finite width κ of the probe pulse. In general, during the interaction with the laser pulse with a frequency of $\omega_0 = 2J$ electrons are excited from $\omega \approx -1J$ to $\omega \approx 1J$. The precise shape of the excited carrier

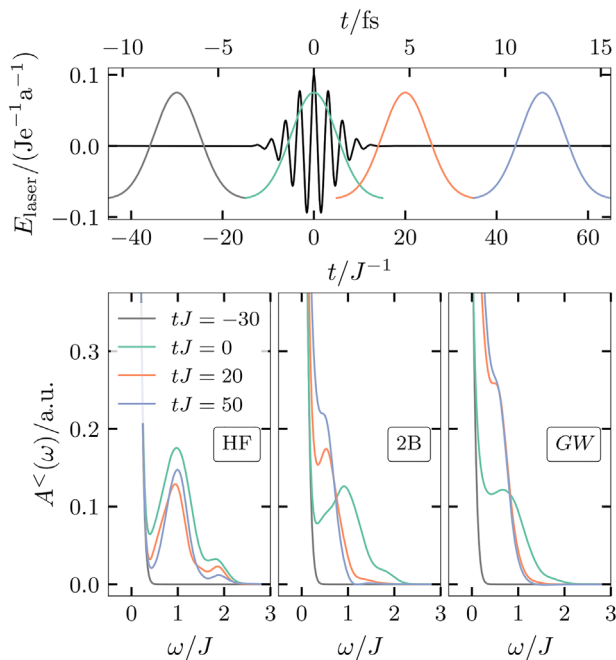


Figure 7. The lower panels show the time-dependent photoemission spectrum for a 5-AGNR with a length of $L = 6$ at four different times before, during and after a laser excitation for the HF (left), 2B (middle), and GW (right) self-energy at $U = 3.5J$. In the upper panel, the four times are marked, with respect to the pump laser pulse (black line), by Gaussian functions that correspond to the probe pulse.

distribution differs slightly for the distinct self-energies which is likely due to the different descriptions of the band structure and the resulting possible single-particle transitions. Nevertheless, the direct single-particle excitation by the laser pulse is already well reproduced by the HF self-energy.

However, for the correct description of the electron dynamics after the laser pulse correlation effects have to be included. For the HF self-energy the total spectral weight in the conduction band ($\omega > 0$) decreases slightly after the laser-pulse amplitude vanishes. However, the general shape of the distribution remains the same because collision processes that could lead to a redistribution of the occupation are not contained in the mean-field description. In contrast, using the 2B self-energy that takes into account collision events between electrons a considerable shift of the excited carrier occupation can be observed after the laser-pulse interaction. Even for long times (≈ 12 fs) after the excitation the system has not reached a steady state yet. Instead, the number of particles in the valence band seems to increase. One possible explanation for this are carrier multiplication effects that were predicted^[73–76] and experimentally observed^[20,22,77,78] for various graphene structures. In this mechanism, highly-excited electrons can excite additional electrons from the valence to the conduction band through collisions. In total this results in an increase of the carrier density in the conduction band but a decrease of their mean energy. This effect will be studied in greater detail in a forthcoming paper.

The GW approximation observes a similar redistribution of the excited carriers toward lower energies with a simultaneous increase in the electron density. However, between $tJ = 20$ and

$tJ = 50$ this effect is considerably smaller than for the 2B self-energy. Nonetheless, both the 2B and the GW self-energy contain electron–electron collision effects which lead to the increase of carriers in the conduction band. Since HF does not include these kind of scattering events, going beyond the mean-field level is essential for the correct description of the observed electron dynamics. Therefore, previously developed extended TB and mean-field models^[46,79,80] are not suitable for the electron dynamics considered here.

5. Conclusions and Outlook

In this paper, we have developed a new approach to describe the time-resolved nonequilibrium dynamics and spectral properties of finite graphene nanoclusters. Our description is based on an extension of the standard Hubbard model that is solved by the nonequilibrium Green functions (NEGF) approach to include correlations. Due to its concise nature the Hubbard model greatly reduces the computational demands of the description of finite systems. For the correct description of finite graphene nanostructures the standard Hubbard model has to be extended to take into account the overlap of the π -orbitals in the graphene honeycomb lattice. Here, hopping and overlap between up to third-nearest neighbors is included. The parameter set is taken from Tran et al.^[36] that was created to accurately describe finite graphene systems. Additionally, to determine the on-site interaction U the band gap and band structure of a 7-AGNR has been compared to various theoretical and experimental results.^[12,26,68–70] It was found that the width of the band gap of 7-AGNRs on Au(111) is well reproduced using the GW self-energy and an interaction of $U = 3.5J$.

Furthermore, we investigated the response of a 5-AGNR with a length of $L = 6$ to a laser-pulse excitation and compared the results of the HF, 2B, and GW self-energies. Taking correlation effects into account appeared to be mandatory for the correct description of the electron dynamics in the nanoribbon following the laser pulse interaction. On the mean-field level the general shape of the electron distribution in the conduction band did not change for long times (≈ 12 fs) after the laser pulse excitation. In contrast for the 2B and GW self-energy an increase of the particle number in the upper band was observed even after the interaction with the laser has vanished. This could indicate the presence of carrier multiplication effects that will be further investigated in an upcoming paper.

The flexibility of the presented approach allows us to describe not only GNRs but finite graphene structures in general with any possible lattice geometry. In fact, there is a variety of systems with different edge structures that exhibit intriguing properties^[7,81–83] that could be analyzed using this model in the future. One interesting system is carbon nanotubes (CNTs) which have a similar structure to GNRs.^[84] In the presented approach of the extended Hubbard model and the NEGF method CNTs can be described as GNRs with periodic boundary conditions perpendicular to the ribbon axis. Therefore, it is easy to also extend the investigations to CNTs. Of course, the parameter set might have to be adjusted if the systems differ strongly from the GNRs considered here.

Conflict of Interest

The authors declare no conflict of interest.

Keywords

correlated dynamics, graphene nanoribbons, Hubbard model, nonequilibrium Green functions

Received: September 21, 2018

Revised: November 9, 2018

Published online:

-
- [1] K. S. Novoselov, A. K. Geim, S. V. Morozov, D. Jiang, Y. Zhang, S. V. Dubonos, I. V. Grigorieva, A. A. Firsov, *Science* **2004**, 306, 666.
- [2] P. Avouris, Z. Chen, V. Perebeinos, *Nat. Nanotechnol.* **2007**, 2, 605.
- [3] X. Wang, L. Zhi, K. Müllen, *Nano Lett.* **2008**, 8, 323.
- [4] Y. H. Hu, H. Wang, B. Hu, *ChemSusChem* **2010**, 3, 782.
- [5] I. V. Lightcap, P. V. Kamat, *Acc. Chem. Res.* **2013**, 46, 2235.
- [6] Y. Song, S. Chang, S. Gradecak, J. Kong, *Adv. Energy Mater.* **2016**, 6, 1600847.
- [7] M. Dvorak, W. Oswald, Z. Wu, *Sci. Rep.* **2013**, 3, 2289.
- [8] S. Y. Zhou, G. H. Gweon, A. V. Fedorov, P. N. First, W. A. de Heer, D. H. Lee, F. Guinea, A. H. Castro Neto, A. Lanzara, *Nat. Mater.* **2007**, 6, 770.
- [9] C. Jeon, H. C. Shin, I. Song, M. Kim, J. H. Park, J. Nam, D. H. Oh, S. Woo, C. C. Hwang, C. Y. Park, J. R. Ahn, *Sci. Rep.* **2013**, 3, 2725.
- [10] F. Guinea, M. I. Katsnelson, A. K. Geim, *Nat. Phys.* **2009**, 6, 30.
- [11] S. M. Choi, S. H. Jhi, Y. W. Son, *Phys. Rev. B* **2010**, 81, 081407.
- [12] L. Yang, C. H. Park, Y. W. Son, M. L. Cohen, S. G. Louie, *Phys. Rev. Lett.* **2007**, 99, 186801.
- [13] M. Y. Han, B. Özyilmaz, Y. Zhang, P. Kim, *Phys. Rev. Lett.* **2007**, 98, 206805.
- [14] J. Bai, X. Duan, Y. Huang, *Nano Lett.* **2009**, 9, 2083.
- [15] L. Jiao, X. Wang, G. Diankov, H. Wang, H. Dai, *Nat. Nanotechnol.* **2010**, 5, 321.
- [16] O. V. Yazyev, *Acc. Chem. Res.* **2013**, 46, 2319.
- [17] A. Kimouche, M. M. Ervasti, R. Drost, S. Halonen, A. Harju, P. M. Joensuu, J. Sainio, P. Liljeroth, *Nat. Commun.* **2015**, 6, 10177.
- [18] R. M. Jacobberger, B. Kiraly, M. Fortin-Deschenes, P. L. Levesque, K. M. McElhinny, G. J. Brady, R. Rojas Delgado, S. Singha Roy, A. Mannix, M. G. Lagally, P. G. Evans, P. Desjardins, R. Martel, M. C. Hersam, N. P. Guisinger, M. S. Arnold, *Nat. Commun* **2015**, 6, 8006.
- [19] S. A. Jensen, R. Ulbricht, A. Narita, X. Feng, K. Müllen, T. Hertel, D. Turchinovich, M. Bonn, *Nano Lett.* **2013**, 13, 5925.
- [20] I. Gierz, J. C. Petersen, M. Mitrano, C. Cacho, I. C. E. Turcu, E. Springate, A. Stöhr, A. Köhler, U. Starke, A. Cavalleri, *Nat. Mater.* **2013**, 12, 1119.
- [21] R. Denk, M. Hohage, P. Zeppenfeld, J. Cai, C. A. Pignedoli, H. Söde, R. Fasel, X. Feng, K. Müllen, S. Wang, D. Prezzi, A. Ferretti, A. Ruini, E. Molinari, P. Ruffieux, *Nat. Commun.* **2014**, 5, 5253.
- [22] I. Gierz, F. Calegari, S. Aeschlimann, M. Chávez Cervantes, C. Cacho, R. T. Chapman, E. Springate, S. Link, U. Starke, C. R. Ast, A. Cavalleri, *Phys. Rev. Lett.* **2015**, 115, 086803.
- [23] G. Soavi, S. D. Conte, C. Manzoni, D. Viola, A. Narita, Y. Hu, X. Feng, U. Hohenester, E. Molinari, D. Prezzi, K. Müllen, G. Cerullo, *Nat. Commun.* **2016**, 7, 11010.
- [24] B. V. Senkovskiy, A. V. Fedorov, D. Haberer, M. Farjam, K. A. Simonov, A. B. Preobrajenski, N. Mårtensson, N. Atodiresei, V. Caciuc, S. Blügel, A. Rosch, N. I. Verbitskiy, M. Hell, D. V. Evtushinsky, R. German, T. Marangoni, P. H. M. van Loosdrecht, F. R. Fischer, A. Grüneis, *Adv. Electron. Mater.* **2017**, 3, 1600490.
- [25] I. Ivanov, Y. Hu, S. Osella, U. Beser, H. I. Wang, D. Beljonne, A. Narita, K. Müllen, D. Turchinovich, M. Bonn, *J. Am. Chem. Soc.* **2017**, 139, 7982.
- [26] S. Wang, L. Talirz, C. A. Pignedoli, X. Feng, K. Müllen, R. Fasel, P. Ruffieux, *Nat. Commun.* **2016**, 7, 11507.
- [27] D. J. Rizzo, G. Veber, T. Cao, C. Bronner, T. Chen, F. Zhao, H. Rodriguez, S. G. Louie, M. F. Crommie, F. R. Fischer, *Nature* **2018**, 560, 204.
- [28] L. Keldysh, *Soviet Phys. JETP* **1965**, 20, 1018 [Zh. Eksp. Teor. Fiz. **1964**, 47, 1515].
- [29] M. Bonitz, A. Jauho, M. Sadovskii, S. Tikhodeev, **2018**, submitted for publication, this issue.
- [30] N. Schlünzen, J. P. Joost, F. Heidrich-Meisner, M. Bonitz, *Phys. Rev. B* **2017**, 95, 165139.
- [31] N. Schlünzen, J. P. Joost, M. Bonitz, *Phys. Rev. B* **2017**, 96, 117101.
- [32] N. Schlünzen, M. Bonitz, *Contrib. Plasma Phys.* **2016**, 56, 5.
- [33] R. Saito, G. Dresselhaus, M. Dresselhaus, *Physical Properties of Carbon Nanotubes*. Imperial College Press, **1998**.
- [34] J. Munárriz Arrieta, *Modelling of Plasmonic and Graphene Nano-devices*. Springer International Publishing, Cham **2014**, Ch 2.
- [35] S. Reich, J. Maultzsch, C. Thomsen, P. Ordejón, *Phys. Rev. B* **2002**, 66, 035412.
- [36] V. T. Tran, J. Saint-Martin, P. Dollfus, S. Volz, *AIP Adv.* **2017**, 7, 075212.
- [37] P. O. Löwdin, *J. Chem. Phys.* **1950**, 18, 365.
- [38] R. Kundu, *Mod. Phys. Lett. B* **2011**, 25, 163.
- [39] D. Neilson, A. Perali, M. Zarenia, *J. Phys.: Conf. Ser.* **2016**, 702, 012008.
- [40] D. Prezzi, D. Varsano, A. Ruini, A. Marini, E. Molinari, *Phys. Rev. B* **2008**, 77, 041404.
- [41] T. Helgaker, P. Jørgensen, J. Olsen, *Molecular Electronic-Structure Theory*. John Wiley & Sons Ltd, Chichester **2000**.
- [42] P. R. Surján, *Second Quantized Approach to Quantum Chemistry*. Springer-Verlag, Berlin **1989**.
- [43] C. C. J. Roothaan, *Rev. Mod. Phys.* **1951**, 23, 69.
- [44] G. G. Hall, *Proc. R. Soc. London, Ser. A* **1951**, 205, 541.
- [45] K. I. Ramachandran, G. Deepa, K. Namboori, *Computational Chemistry and Molecular Modeling*. Springer-Verlag, Berlin **2008**.
- [46] Y. Hancock, A. Uppstu, K. Saloritta, A. Harju, M. J. Puska, *Phys. Rev. B* **2010**, 81, 245402.
- [47] G. Stefanucci, R. v. Leeuwen, *Nonequilibrium Many-Body Theory of Quantum Systems: A Modern Introduction*. Cambridge University Press, Cambridge **2013**.
- [48] K. Balzer, M. Bonitz, *Nonequilibrium Green's Functions Approach to Inhomogeneous Systems*. Lect. Notes Phys., Vol. 867, Springer, Berlin, Heidelberg **2013**.
- [49] Of course there are experimental observations^[26] and mean field level calculations^[85,86] that exhibit spin asymmetries in the form of so-called edge states. However, those are only single measurements in the case of the experiments and (known but often times ignored) shortcomings of the HF approach which breaks the SU(2)-symmetry of the Hubbard model. The Green function is ensemble averaged and provides the expectation value instead of single measurements of observables such as the density which is clearly symmetric with respect to the spin.^[87]
- [50] M. Eckstein, M. Kollar, *Phys. Rev. B* **2008**, 78, 245113.
- [51] R. C. Albers, N. E. Christensen, A. Svane, *J. Phys.: Condens. Matter* **2009**, 21, 343201.
- [52] G. Baym, L. P. Kadanoff, *Phys. Rev.* **1961**, 124, 287.
- [53] M. Bonitz, S. Hermanns, K. Balzer, *Contrib. Plasma Phys.* **2013**, 53, 778.
- [54] S. Hermanns, N. Schlünzen, M. Bonitz, *Phys. Rev. B* **2014**, 90, 125111.
- [55] D. Lacroix, S. Hermanns, C. M. Hinz, M. Bonitz, *Phys. Rev. B* **2014**, 90, 125112.

- [56] M. P. von Friesen, C. Verdozzi, C. O. Almbladh, *Phys. Rev. Lett.* **2009**, 103, 176404.
- [57] M. P. von Friesen, C. Verdozzi, C. O. Almbladh, *Phys. Rev. B* **2010**, 82, 155108.
- [58] P. Romaniello, F. Bechstedt, L. Reining, *Phys. Rev. B* **2012**, 85, 155131.
- [59] M. Gatti, F. Bruneval, V. Olevano, L. Reining, *Phys. Rev. Lett.* **2007**, 99, 266402.
- [60] A. N. Chantis, M. van Schilfhaarde, T. Kotani, *Phys. Rev. B* **2007**, 76, 165126.
- [61] S. Hermanns, Phd thesis, Christian-Albrechts-Universität zu Kiel **2016**.
- [62] N. E. Dahlen, R. van Leeuwen, *J. Chem. Phys.* **2005**, 122, 164102.
- [63] A. Stan, R. van Leeuwen, *J. Chem. Phys.* **2009**, 130, 224101.
- [64] The most demanding simulations performed in the scope of this work have been done for systems of 30 Hubbard sites and a propagation time of $110J^{-1}$ using a time step of $\Delta 0.01J^{-1}$. For the GW self-energy such simulations would typically take around seven days to complete on a single NVIDIA Tesla P100 and use up to 300GB of RAM each. Using the 2B self-energy reduces the time of the calculation to about two days while the memory consumption stays the same.
- [65] M. Scharnke, N. Schlünzen, M. Bonitz, *J. Math. Phys.* **2017**, 58, 061903.
- [66] M. Bonitz, M. Scharnke, N. Schlünzen, *Contrib. Plasma Phys.* **2018**, 58, 1036.
- [67] N. Schlünzen, S. Hermanns, M. Bonitz, C. Verdozzi, *Phys. Rev. B* **2016**, 93, 035107.
- [68] Y. W. Son, M. L. Cohen, S. G. Louie, *Phys. Rev. Lett.* **2006**, 97, 216803.
- [69] P. Ruffieux, J. Cai, N. C. Plumb, L. Patthey, D. Prezzi, A. Ferretti, E. Molinari, X. Feng, K. Müllen, C. A. Pignedoli, R. Fasel, *ACS Nano* **2012**, 6, 6930.
- [70] H. Söde, L. Talirz, O. Gröning, C. A. Pignedoli, R. Berger, X. Feng, K. Müllen, R. Fasel, P. Ruffieux, *Phys. Rev. B* **2015**, 91, 045429.
- [71] J. P. Joost, Master's thesis, Christian-Albrechts-Universität zu Kiel **2017**.
- [72] P. E. Trevisanutto, C. Giorgetti, L. Reining, M. Ladisa, V. Olevano Ab Initio, *Phys. Rev. Lett.* **2008**, 101, 226405.
- [73] T. Winzer, A. Knorr, E. Malic, *Nano Lett.* **2010**, 10, 4839.
- [74] R. Baer, E. Rabani, *Nano Lett.* **2010**, 10, 3277.
- [75] S. Konabe, N. Onoda, K. Watanabe, *Phys. Rev. B* **2010**, 82, 073402.
- [76] F. Schulze, M. Schoth, U. Woggon, A. Knorr, C. Weber, *Phys. Rev. B* **2011**, 84, 125318.
- [77] N. M. Gabor, Z. Zhong, K. Bosnick, J. Park, P. L. McEuen, *Science* **2009**, 325, 1367.
- [78] S. Wang, M. Khafizov, X. Tu, M. Zheng, T. D. Krauss, *Nano Lett.* **2010**, 10, 2381.
- [79] Y. Wu, P. Childs, *Nanoscale Res. Lett.* **2010**, 6, 62.
- [80] T. Stegmann, J. A. Franco-Villafañe, U. Kuhl, F. Mortessagne, T. H. Seligman, *Phys. Rev. B* **2017**, 95, 035413.
- [81] D. G. de Oteyza, A. García-Lekue, M. Vilas-Varela, N. Merino-Díez, E. Carbonell-Sanromà, M. Corso, G. Vasseur, C. Rogero, E. Guitián, J. I. Pascual, J. E. Ortega, Y. Wakayama, D. Peña, *ACS Nano* **2016**, 10, 9000.
- [82] G. D. Nguyen, H. Z. Tsai, A. A. Omrani, T. Marangoni, M. Wu, D. J. Rizzo, G. F. Rodgers, R. R. Cloke, R. A. Durr, Y. Sakai, F. Liou, A. S. Aikawa, J. R. Chelikowsky, S. G. Louie, F. R. Fischer, M. F. Crommie, *Nat. Nanotechnol.* **2017**, 12, 1077.
- [83] C. Bronner, R. A. Durr, D. J. Rizzo, Y. L. Lee, T. Marangoni, A. M. Kalayjian, H. Rodriguez, W. Zhao, S. G. Louie, F. R. Fischer, M. F. Crommie, *ACS Nano*, **2018**, 12, 2193.
- [84] J. C. Charlier, X. Blase, S. Roche, *Rev. Mod. Phys.* **2007**, 79, 677.
- [85] H. Feldner, Z. Y. Meng, A. Honecker, D. Cabra, S. Wessel, F. F. Assaad, *Phys. Rev. B* **2010**, 81, 115416.
- [86] M. Golor, C. Koop, T. C. Lang, S. Wessel, M. J. Schmidt, *Phys. Rev. Lett.* **2013**, 111, 085504.
- [87] T. Hikihara, X. Hu, H. H. Lin, C. Y. Mou, *Phys. Rev. B* **2003**, 68, 035432.